Multidisciplinary Cooling Design Tool for Electric Vehicle SiC Inverters Utilizing Transient 3D-CFD Computations

eTransportation 7 (2021) 100092

Contents lists available at ScienceDirect

eTransportation

journal homepage: www.journals.elsevier.com/etransportation

Multidisciplinary cooling design tool for electric vehicle SiC inverters utilizing transient 3D-CFD computations

Georgios Mademlis [a, *], Raik Orbay [b], Yujing Liu [a], Nimananda Sharma [a], Rickard Arvidsson [b], Torbjörn Thiringer [a]

[a] Department of Electrical Engineering, Division of Electric Power Engineering, Chalmers University of Technology, SE-41296, Gothenburg, Sweden
[b] Volvo Car Corporation Vehicle Propulsion - 97120 Propulsion System Technology, Torslanda PVOSG 31, SE-40531, Gothenburg, Sweden

ARTICLE INFO

Article history:
Received 9 July 2020
Received in revised form
25 October 2020
Accepted 11 November 2020
Available online 19 November 2020

Keywords:
Computational fluid dynamics
Electric vehicles
Liquid cooling
Transient thermal behavior
SiC MOSFET
Temperature uniformity

ABSTRACT

This paper proposes a new design tool that can be used for the development of a proper cooling component for high-power three-phase SiC module-packs for electric vehicles. Specifically, a multidisciplinary approach of the design process is presented that is based on the accurate electrical, thermal and fluid-mechanics modeling as well as computational testing of a high-power three-phase SiC module-pack under transient-load conditions, so that it can effectively meet the highly-demanding cooling requirements of an electric vehicle inverter. The cooling plate is initially designed by using steady-state based 3D-computational-fluid-dynamic (CFD) tool, as in a conventional method. Then, the proposed design algorithm fine-tunes it through transient 3D-CFD computations by following a specific iterative improvement procedure considering the heat dissipation requirements for the SiC power switches during the official driving cycles for passenger vehicles and during abrupt acceleration tests under several ambient environments. Therefore, not only overheating at all operating conditions is avoided, but also, accurate thermal modeling of the individual inverter modules is provided that can be used for lifetime estimations and for calculating the overload capability of the inverter. The design improvement attained with the proposed procedure against the conventional steady-state approach is validated on a traction 450 A SiC inverter with the model of a real passenger vehicle.

1. Introduction

Electrification is one of the most important engineering solutions for environmentally viable universal transports. However, the applicability of the electric propulsion system for mobile usage is still limited due to costs of adoption, drivability and electric range [1]. One way to optimize these attributes is by tuning the on-board cooling system. Therefore, efficient heatsinks of inverters can lead to more compact designs with least possible material expense and long life cycles, and this would allow for a development of more efficient packaging of components for automotive drives [2,3]. Specifically, the inverter design for the drivetrain of passenger battery-electric vehicles (BEV) is a challenging issue, since it requires optimization in the electrical and thermal design of the system as well as taking the operation of the vehicle into consideration.

The operating voltage of the power inverter is an important design parameter with most of today's BEVs having a drivetrain operating at approximately 400 V dc-link voltage [4]. However, there is an increasing demand for vehicles with high acceleration and top speed, which means that motor inverters with even higher power are needed and at the same time keeping the volume and weight as low as possible. Lately automotive car manufacturers are considering to move from a battery voltage of 400 V–800 V. The increase of the dc-bus voltage to 800 V can allow higher drivetrain power improving the acceleration of the vehicle. In case identical power is kept, the current can be reduced and as a consequence the copper losses as well, resulting into increased system efficiency. A higher voltage can also support faster charging rates of the battery [4,5], which has always been one of the main downsides of electric powertrains compared to combustion engines.

For the 800 V systems, 1.2-kV-class power semiconductors with

* Corresponding author. Department of Electrical Engineering, Division of Electric Power Engineering, Chalmers University of Technology, Gothenburg, Sweden.
E-mail address: georgios.mademlis@chalmers.se (G. Mademlis).

https://doi.org/10.1016/j.etran.2020.100092
2590-1168/

SiC can offer distinctive advantages compared to the Si counterparts. SiC MOSFETs can have lower switching losses for given switching frequencies and lower conduction losses due to the absence of a knee voltage in light and medium load conditions compared to Si IGBTs [5,6], which are the most commonly used for BEVs [7]. SiC semiconductors also have the capability to operate at higher coolant temperatures compared to Si devices, which is particularly beneficial for traction applications where a high ambient temperature can typically be observed [8]. Based on these advantages of the SiC technology, the design of an automotive inverter with newly released 450 A SiC power modules is presented in this paper.

In most of the available literature, heatsinks are dimensioned for maximum load at steady-state regime [9]. However, the components may never reach these limits under normal driving conditions in a passenger BEV. Despite this, steady-state physics are often utilized in similar thermal modelling studies [2,10], which does not represent the reality, since the load of the inverter is constantly varying. Therefore, long real-time thermal simulations of the inverter are necessary in order to evaluate the temperatures of the designed system under transient load and to more accurately evaluate its efficiency and reliability. These simulations are usually implemented with equivalent models and single-point representation of the inverter, such as the ones presented in Ref. [11–15]. Large simulation time-step of 1 ms and a simplified thermal network is used in Ref. [11], while a quasi-transient lumped-parameter model is used in Ref. [12] for modelling specific driving cycles. Similarly, an equivalent Cauer network is used in Ref. [13] for thermal modelling of an IGBT chip. A reliability estimation of traction inverters through Matlab modelling is presented in Ref. [14]. The sizing process for the power switches of a BEV IGBT inverter has been presented in Ref. [15], where simulation results from multiple drive cycles are shown. However, the thermal modelling of the IGBT inverter in this article is also simplified, where constant temperature or a single temperature-point is considered. An adaptive lumped RC model has been developed in Ref. [16], where temperature and material dependent thermal parameters are used for long-time simulations. A finite element model of the system is used for the fine-tuning of the parameters; however, the fluid dynamics have not been considered which is important for the design of liquid-cooled heatsinks.

The sizing of the heatsink involves a multidisciplinary approach in order to capture all the physical properties for thermal conditioning of the electric components. The thermal performance of the inverter can be studied more accurately with 3D Conjugate Heat Transfer (CHT) computations, where both fluid and solid elements in thermal contact are handled. The turbulence of the fluid, which is a strictly 3D mechanism, should also be modelled for accurate results. In addition, circuit simulation tools are needed for testing the control of the electric drive and the loss calculation. Finally, driving cycle computations of BEVs show a more dynamic perspective of the vehicle's operation, which is an additional challenge.

Although equivalent thermal modelling can provide information of the inverter temperatures in transient electrical and thermal simulations, the necessary simplifications made, such as considering uniform temperature and loss distribution of the inverter, can introduce errors. A 3D model of the inverter using computational fluid dynamic (CFD) tools can more accurately represent the thermal behavior of the semiconductor devices and the coolant flow. The proposed heatsinks referenced previously in Refs. [17–22] present CFD simulations; however, only the steady state operation of the inverter has been considered. Transient simulations as the ones in Ref. [11–15] are also needed, especially for passenger BEV, where the system operates very seldom at maximum load. However, equivalent thermal models have been used in these papers. Simulation results by utilizing a Cauer thermal model and transient CFD computations have been presented in Ref. [23] for an air-cooled low-powered GaN inverter for some custom 233 s long current profiles. Quasi-transient CFD modelling has also been used in projects where transient 3D simulations are required [24,25]. Coupled 1D and 3D CFD tools have been used in these papers in order to run accelerated simulations. Specifically, the solver of the 1D CFD software computes the transient response of the system, while a coupled 3D model is used for the calculation of the steady-state system parameters at each time-step. Although the computation load is lower with the above method, the results are not as realistic as in the fully transient 3D CFD approach.

From the above it is concluded that an effective and practical thermal design technique specially tuned for the cooling component of automotive SiC high-power inverters is missing from the technical literature. Specifically, time-varying 3D CHT modelling has not been utilized yet as the design tool for the inverter heatsink. Steady-state modelling is preferred, instead, as the general practice by most designers, although it is unsuitable for automotive applications with constantly varying loads. Contrarily, a new dynamic modelling process of the inverter with transient CHT computations could more accurately quantify the flow of the coolant, allowing to fine-tune the design of the inverter.

This paper aims to present a new heatsink design tool based on the transient 3D CHT computation technique, where the cooling plate geometry of a SiC inverter is fine-tuned, so as, to meet the specific needs of an electric vehicle, by following the newly legislated rules for the driving cycles, as per [26,27]. A specific iterative design and computational testing procedure is proposed in order to ensure accurate design and high utilization of the cooling capability of the heatsink, for the proper operation of the SiC inverter under the demanding requirements of an electric vehicle application. The effectiveness and the operation improvements in the cooling design of the automotive SiC inverter are validated by comparing the computation results of the proposed transient 3D CFD method with that obtained by the conventional method that uses the steady-state thermal design technique.

Since the cooling of the inverter is the key point for the safe and seamless operation of an electric vehicle, it is revealed that the proposed transient 3D design technique can be a tailor-cut tool for the above purpose. Furthermore, not only safety is ensured, but also, valuable information for the individual temperature of each power module, the flow of the coolant, the fault mode analysis of the inverter, the attained Nusselt number and the temperature distribution within the heatsink can be acquired. These cannot be obtained with physical measurements by multiple sensors, without affecting the actual system that may result to misleading estimations.

2. Overview of the modelled vehicle drivetrain

The proposed heatsink design tool is validated with the development of a proof-of-concept inverter, where the SiC power modules CAB450M12XM3 from Wolfspeed/Cree are used with maximum voltage and current 1.2 kV and 450 A, respectively [28]. A newly released BEV from a passenger vehicle manufacturing company is also used to provide realistic data for this study.

The SiC inverter developed in this study has been designed to fit the specifications of the test case BEV, whose parameters are summarized in Table 1. Due to the high torque and acceleration of the vehicle, it is classified as a sport car based on [29] and suitable

Table 1
Modelled vehicle technical specifications.

Parameter	Value	Unit
Vehicle mass (empty) m	1900	kg
Dimensions $L \times W \times H$	4.61 × 1.8 × 1.48	m×m×m
Effective area A [29]	2.2879	m^2
Air density ρ_{air}	1.2	kg/m^3
Aerodynamic drag coeffic. C_d [29]	0.35	–
Rolling resistance C_r [29]	0.012	–
Tire size	245/45 R19	–
Wheel radius r	0.35155	m
Acceleration time (0–100 km/h)	6	s
Electric motor arrangement	1 motor, PMSM	–
Maximum torque $T_{m\ max}$	580	Nm
Gear ratio *gear*	5.7	–
Maximum speed v_{max}	209	km/h

parameters for this type of vehicles have been considered.

The acceleration force of the car is defined as [29]

$$F_{acc} = \frac{T_{motor}}{r} gear\, n_{gear} - F_{road\ load} \quad (1)$$

where *gear* is the gear ratio of the transmission system and $F_{road\ load}$ is the load of the wheels. The $F_{road\ load}$ consists of the air drag F_{air}, the rolling resistance F_{roll} and the grading force of the road F_{grade}. These are described as.

$$F_{air} = \frac{1}{2} \rho_{air} C_d A (v_{car} - v_{wind})^2 \quad (2)$$

$$F_{roll} = C_r m g cos(\alpha) \quad (3)$$

$$F_{grade} = m g sin(\alpha) \quad (4)$$

where v_{car} and v_{wind} are the forward speed of the car and the wind, α is the road angle of inclination. For the rest of the paper $v_{wind} = 0$ m/s and $\alpha = 0°$ have been considered. The losses of the gearbox are also not considered in this study, so $n_{gear} = 1$. However, accurate modelling of the powertrain transmission system losses could further increase the accuracy of the electric vehicle model, especially in the case when variable gearbox is used.

The modelled electric drive consists of a three-phase, 2-level inverter and a permanent magnet synchronous motor (PMSM) and its design characteristics will be described in the following Subsection 3.4.

3. SiC automotive inverter design process

The inverter's heatsink of this paper is designed following a multidisciplinary analysis, where the power losses of the SiC MOSFETs and the thermal performance of the cooling plate are determined with both constant and variable load, when a specific driving profile is analysed. A combination of different simulation tools has been used in order to cover all the important aspects of the inverter and the electric motor of the drive, including the electric modelling and control (on Matlab/PLECS), electromagnetic design of the motor, and thermal behavior of the inverter (on Matlab/PLECS and OpenFOAM). A flowchart of the developed design process is shown in Fig. 1 and the iterative process of the heatsink design is analysed in the following subsection.

3.1. Iterative design process of inverter heatsink

Firstly, the needed thermal dissipation power of the inverter's heatsink is defined with a Matlab/PLECS analysis for constant load

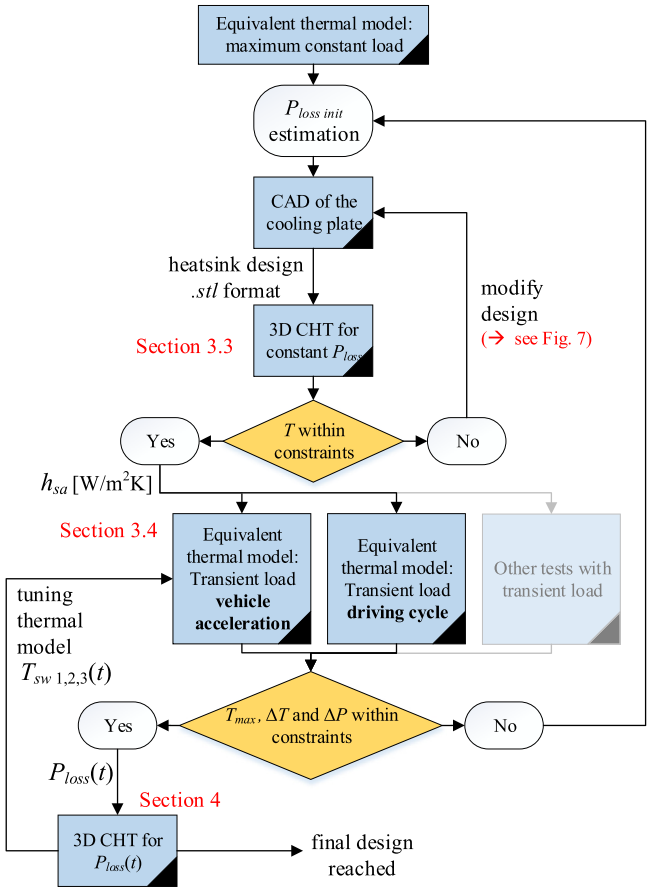

Fig. 1. Flowchart of the inverter's heatsink design process adopting an equivalent thermal and electric model and 3D CHT analysis.

of the drive. Drive operation close to its maximum power can serve as a starting point for the iterative design process calculating the losses at the worst-case conditions for the inverter. The initial thermal properties of the cooling plate are decided with a hand-computed Nusselt number based approach [30]. The required thermal dissipation power $P_{loss\ init}$ is calculated during this design step, where the first draft of the heatsink design will be based on. The $P_{loss\ init}$ is being updated during later steps of the iterative design process and a more accurate value is later defined, as shown in Fig. 1.

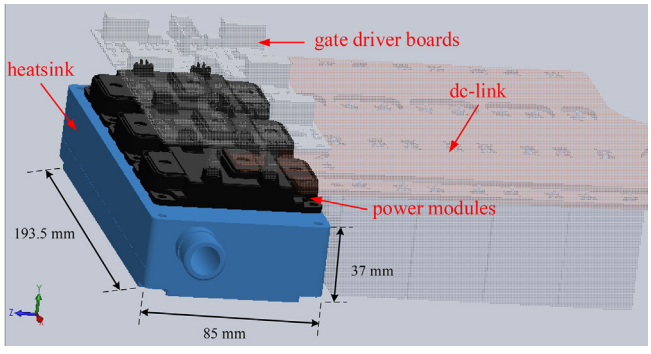

Fig. 2. CAD drawing of the designed inverter with the heatsink highlighted and its outer dimensions shown.

Afterwards, a Computer Aided Design (CAD) of the heatsink is prepared for further computations, as shown in Fig. 2 with the outer dimensions of the cooling plate shown and the connections for the dc-link capacitors and the gate-driver boards. A full 3D CHT model of the heatsink is then used in the next step using the software OpenFOAM, where the performance of the design is evaluated for various operating conditions of the fluid, such as different flow speeds and cooling media temperatures. In case the designed heatsink fulfills the requirements of the specific application (e.g. the temperature of the inverter lays withing the predefined safety limits), the design process moves to the next step which includes testing of the inverter with transient load.

The results of the steady-state 3D analysis are utilized to build a simplified thermal network model of the inverter, where the power losses at various operating points can be calculated. Many driving patterns of the BEV can be tested here with the modelled motor drive, such as an acceleration of the car from standstill up to its maximum speed or legislative driving cycles, which represent the average driving habits of a usual driver. If the calculated temperatures of the power modules during these tests lay within the recommended operating conditions defined by the MOSFET manufacturer, the power loss profile is used by the 3D model of the heatsink to run transient CHT computations with the same load patterns, where the individual temperature of each power module can be obtained. In case the calculated temperatures or the pressure drop of the heatsink's coolant lay outside the design specifications, the design process is repeated, updating accordingly the value of $P_{loss\ init}$ in the first step of the flowchart. The heatsink design is refined by this algorithm with the constant- and transient-load tests until all the design specifications are fulfilled.

An example of the proposed design methodology is presented in the rest of the paper where an automotive inverter heatsink is designed. The following subsections analyze each individual design step starting with the selection of the optimal cooling plate geometry using steady-state CHT models and proceeding with transient CHT computations, where the lifetime of the developed system is also evaluated.

The design process using transient 3D CHT computations is compared with the conventional steady-state design technique and the results demonstrate the advantages of the proposed strategy. Due to the entailed difficulty to measure and verify experimentally thermal parameters such as the heatsink temperature and the inner coolant flow, special care has been taken to follow the exactly same conditions during steady-state and time-dependent computations in order to have a fair comparison. These are for example the boundary conditions, the coolant properties and the mathematical schemes used for the computations.

3.2. Automatized CHT computation for constant or transient heat dissipation

Thermal lumped-parameter-network (LPN) models for components comprising fully developed turbulent flows may not be able to capture all the physics, which depend on how the Biot number is handled [31]. In this project a full 3D CFD model is used to design the heatsink of the inverter.

The solver is the *chtMultiRegionSimpleFoam* from the OpenFOAM toolbox [32] for steady-state computations and the *chtMultiRegionFoam* from Helyx (an OpenFOAM-based CFD tool) for transient cases. As described in the solver header, this is a transient solver for buoyant, turbulent fluid flow and solid heat conduction with conjugate heat transfer between solid and fluid regions.

The following equation set is used by the chosen CFD solver. The fluid domain continuity is handled as

$$\frac{\partial \rho}{\partial t} + \nabla \cdot (\rho \boldsymbol{u}) = 0 \tag{5}$$

where $\boldsymbol{u}$ is the velocity vector and ρ is the fluid density and t is the time variable. Subsequently, the momentum in the fluid domain is modelled by the Navier-Stokes equation in 3D as [33].

$$\frac{\partial(\rho \boldsymbol{u})}{\partial t} + \nabla \cdot (\rho \boldsymbol{u}\boldsymbol{u}) + \nabla \cdot (\mu \nabla \boldsymbol{u}) + \nabla \cdot \left(\mu \left[(\nabla \boldsymbol{u})^T - \frac{2}{3} tr(\nabla \boldsymbol{u})^T \boldsymbol{I} \right] \right) = -\nabla p + \rho \boldsymbol{f} \tag{6}$$

where $\boldsymbol{f}$ is the body force vector, p is the pressure, μ denotes the dynamic viscosity of the cooling fluid. The operator tr in (6) calculates the trace of a tensor in 3 dimensions.

The investigated computational domain comprises individual meshes for the coolant and the heat sink, as shown in Fig. 3(a). The coolant is a mixture of 50% water and 50% ethylene glycol and the solid material is aluminium. The mass, material, inlet/outlet dimensions of the heatsink are provided by the CAD drawing of the heatsink. The exchange of energy is modelled in both domains; in the fluid as [34,35].

$$\frac{\partial(\rho h)}{\partial t} + \nabla \cdot (\rho \boldsymbol{u} h) + \frac{\partial(\rho k)}{\partial t} + \nabla \cdot (\rho \boldsymbol{u} k) - \frac{\partial p}{\partial t} = \rho \boldsymbol{u} \cdot \boldsymbol{g} + \nabla \cdot \left(\alpha_{eff} \nabla h \right) + \rho r \tag{7}$$

where h is the enthalpy of the coolant. The enthalpy is the sum of internal energy of the fluid system and its work on its boundaries. The term r represents the source terms from the radiation heat transfer. Also, k is the kinetic energy of the cooling fluid. The term α_{eff} is the sum of laminar and turbulent thermal diffusivities. Thermal diffusivity α is $\frac{\kappa}{c_p}$, while κ is the thermal conductivity of the coolant and c_p is the specific heat of the material at constant pressure. Finally, the energy equation in the solid is modelled as

$$\frac{\partial \left(\rho_s c_p T \right)}{\partial t} - \nabla(\kappa \nabla T) = 0 \tag{8}$$

where κ is the thermal conductivity and ρ_s the density of the metal [32]. Another important process in convective heat transfer is the turbulence, which is modelled using the $k-\omega$ SST model [36].

For the creation of the computational meshes, the hexahedral-dominant volume mesher from OpenFOAM is used. The rule of thumb for the project was to keep a uniform mesh size throughout the domain. Wall functions are used for near-wall treatment. Both the meshing and computations are parallelized on 480 CPU cores for the transient load cases. For the stability of the computations

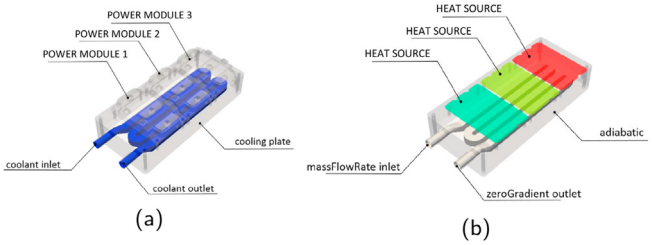

Fig. 3. First investigated heatsink candidate showing (a) the cooling plate (grey) and the cooling circuit (blue) and (b) the boundary conditions for automatized parallel Conjugate Heat Transfer (CHT) modelling of the heatsink. (For interpretation of the references to colour in this figure legend, the reader is referred to the Web version of this article.)

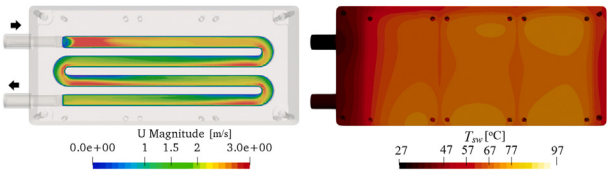

Fig. 4. Initial heatsink design candidate with a 2-loop cooling channel.

appropriate time step-size is chosen and for this purpose Courant number <1 condition is forced to the simulation domain.

High-current power modules, such as the one modelled in this paper, consist of multiple parallel-connected dies which may create local hotspots at the surface of the copper substrate due to the uneven heat flux in the internal direct-bonded-copper (DBC) layers [37]. The exact dimensions of the module inner structure are usually not disclosed and, also, since the focus of this paper is to present explicitly the thermal properties caused by the heatsink design process, the non-uniformities of the power module structure have not been included in the model. Therefore, the boundary conditions are designed so as to represent the three power modules of the three-phase inverter as surface patches that have an evenly distributed heat source with total power being the power losses of the modules. The average temperature on these surface patches is named T_{sw1}, T_{sw2} and T_{sw3}. The set-up is shown in Fig. 3(b).

3.3. Heatsink design with constant heat dissipation

The main objectives for the heatsink is the design to have a good heat dissipation ability and small pressure drop. The candidate designs have also been investigated for uniform heat dissipation, so that the case-surfaces of all the three power modules have similar temperature and, therefore, the same aging. At this step of the design process the heatsink is simulated with constant heat dissipation. A total power loss of 4 kW has been selected for all the three power modules and coolant flow speeds vary between 2.5 l/min and 10 l/min.

Several alternative designs of the heatsink have been compared and the design process has gone through multiple iterations until reaching the optimal result. Conforming with the page restrictions, two characteristic examples are shown in the following figures with the first one being a very standard heatsink design with a two-loop cooling channel shown in Figs. 3 and 4 [22]. The results in Figs. 4 and 5 are shown for a total power loss of 4 kW for all the three power modules and coolant volume flow of 10 l/min. The inlet and outlet of the coolant are indicated with arrows. Although the first heatsink design has a satisfactory thermal performance, its main disadvantage is its large pressure drop and also the inhomogenous temperature among the three MOSFET patches, since the heat dissipation into the coolant creates a temperature gradient on the base-plate of the cooling plate.

Heatsink geometries with pins have been studied and are presented in Fig. 5. Rectangular pins are used due to their simpler and cheaper design, since they can be machined [19], and their better thermal performance [38]. Oppositely, circular pins or other shapes need molding or special manufacturing processes [19], which increases the cost and complexity. Preliminary heatsink versions are shown in Fig. 5(a)–(b), where the number of pins, their positions and other parameters are optimized through an iterative process. The final heatsink design with a more homogenous temperature distribution per MOSFET patch and overall thermal performance is shown in Fig. 5(c), which has been chosen for further steps of the design process.

Comparative results from the steady-state CHT computations

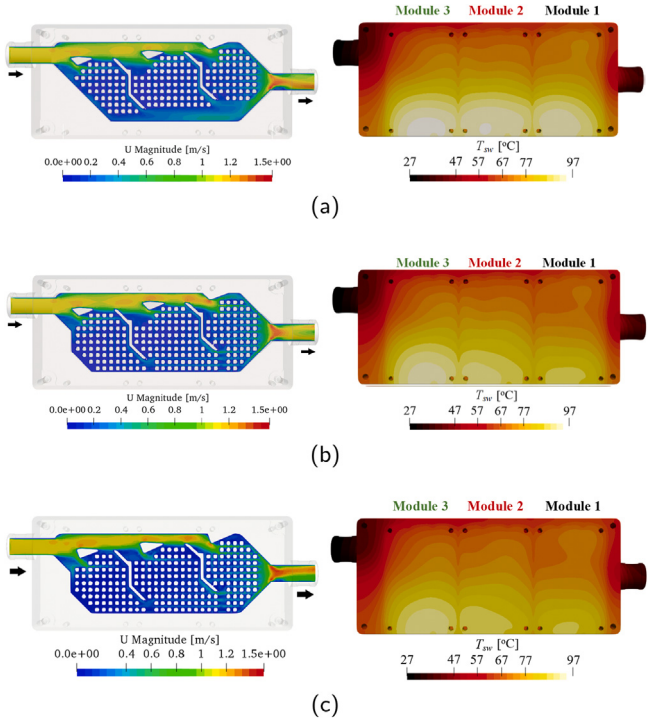

Fig. 5. Heatsink designs with multiple rectangular pins and three straight fins dividing the flow into equal sections: (a)–(b) preliminary designs and (c) final selected geometry.

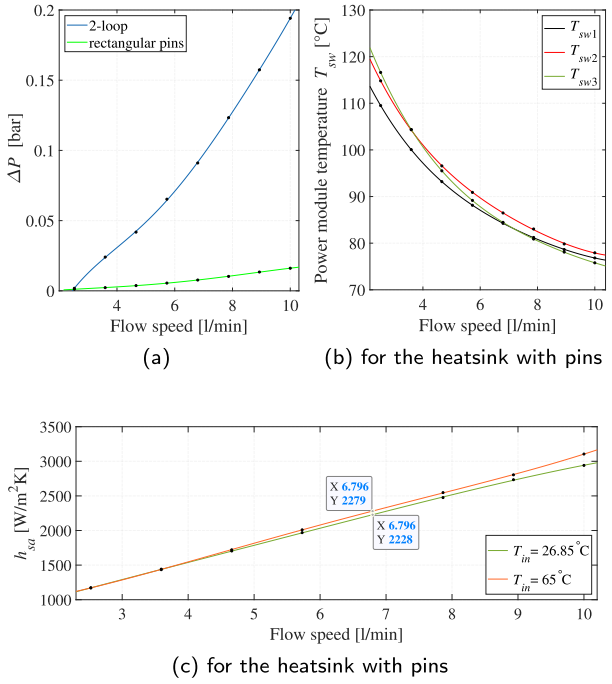

Fig. 6. 3D CHT results showing the (a) pressure drop between inlet and outlet; (b) average temperature of the power module patches for T_{in} = 26.85 °C and (c) the heat transfer coefficient between sink-coolant for the chosen heatsink with rectangular pins (for reference temperature equal to T_{in}).

can be found in Fig. 6 for both alternative heatsink designs. Specifically, the pressure drop between inlet-outlet is shown for all the designs in Fig. 6(a), while the average temperature of each power

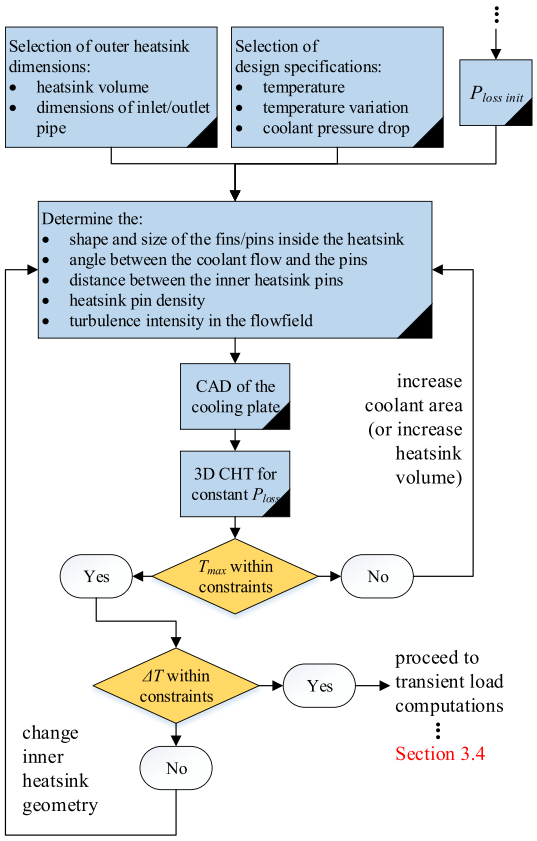

Fig. 7. Flowchart of the constant load design step for heatsink accommodating multiple pins.

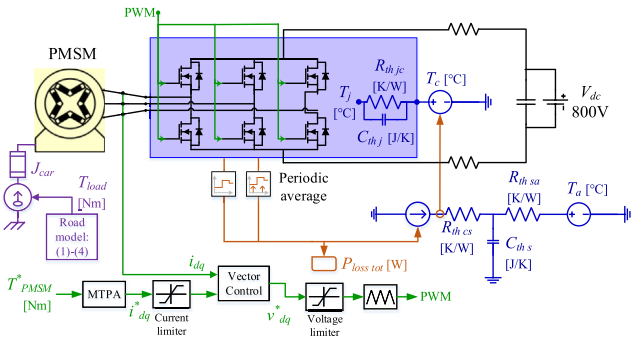

Fig. 8. Schematic of the electric drive including the simplified thermal network model of the inverter and the loss calculation block.

Table 2
Electric drive parameters.

Parameter	Value	Unit
Number of pole pairs p	4	–
Rotor rotational inertia J_{PMSM}	0.018	kg/m^2
Stator resistance R_s	0.026	Ω
Maximum rotor speed n_{max}	9000	rpm
No-load stator inductance L_d	0.90	mH
No-load stator inductance L_q	2.61	mH
Nominal dc-link voltage V_{dc}	800	V
DC-link capacitance C_{dc}	480	μF
Switching frequency f_{sw}	10	kHz
External gate resistance R_G	1	Ω
Current controller bandwidth α_I	1000	rad/s
Cooling channel area A_c (for heatsink with pins)	0.060442	m^2
Specific heat capacity of Al c_p	910	J/(K kg)
Case-sink thermal resist. $R_{th\ cs\ sw}$ [39]	0.026	K/W
Cooling plate with pins mass m_h	1.3606	kg

module patch for the second heatsink design with pins is shown in Fig. 6(b). The heat transfer coefficient between the sink and the coolant h_{sa} is shown also in Fig. 6(c) when the temperature of the coolant at the inlet is $T_{in} = 26.85$ °C and 65 °C, representing operation of the inverter at cool and warmer environments, respectively. The reference temperature for the h_{sa} is the inlet coolant temperature in both cases.

The flowchart in Fig. 7 summarizes the iterative design process of the heatsink with rectangular pins, when the inverter is tested with constant load. The design specifications and the desired heatsink dimensions are firstly determined, as well as the targeted power loss dissipation at constant load $P_{loss\ init}$. Afterwards, multiple design iterations are conducted, where many design variables are optimized until the maximum temperature and the temperature variation at the surface of the sink lay within the desired constraints. The optimized heat transfer coefficient of the heatsink h_{sa} is also calculated, since it is used in the inverter model of the next subsection.

3.4. Inverter loss calculation with a Thermo-electric system model

The modelled electric drive is shown in Fig. 8 and in Table 2. Since the power modules CAB450M12XM3 are used for the inverter, a maximum AC current of 450 A (peak) can be produced for the chosen switching frequency, according to the datasheet of that product (for the case temperature $T_c = 90°$ and junction temperature $T_j = 175°$).

The PMSM used in this study is an up-scaled model of a real traction motor shown in Fig. 9(a). A 2D finite element model (FEM) of the machine is created in ANSYS Maxwell. The specifications of the motor did not fit the requirements of the drive considered in this paper, since the peak current was 332 A and operated with an inverter of 360 V dc-link voltage. Therefore, the stack length in the FEM model has been up-scaled by a factor of two. This will increase the flux linkage linearly increasing the torque and the back-EMF voltage and will result into a machine model suitable for simulation with 800 V dc-link voltage and higher peak torque. Increasing the voltage will have an impact on the insulation of the windings, which is not considered here. The look-up-table-based flux linkage maps ψ_d and ψ_q [Fig. 9(b)] generated from the FEM model are then used along with the parameters listed in Table 2 to model the motor in Matlab/PLECS. The PMSM losses have not been considered in this study, since the focus is on the semiconductor losses of the inverter.

Using the flux linkages calculated from the FEM model and applying the voltage and current constraints, the current reference maps as shown in Fig. 9(c) and (d) are generated. Maximum Torque per Ampere (MTPA) is used [40], when the rotational speed is lower than the base-speed, and flux-weakening with Maximum Torque per Voltage (MTPV) is applied for higher speeds as current reference selection strategy. The motor operates in torque control mode and the gains of the current controller are dimensioned based on the Loop Shaping method [41]. Since the maximum speed of the specific PMSM is $n_{max} = 9000$ rpm, the maximum speed in km/h that the vehicle can attain is equal to $v_{max} = 209$ km/h.

As seen in Fig. 8, except for the rotor inertia of the PMSM, the inertia due to the mass of the vehicle m is considered, which converted to the motor side is calculated as

$$J_{car} = \frac{m\,r^2}{gear^2} \tag{9}$$

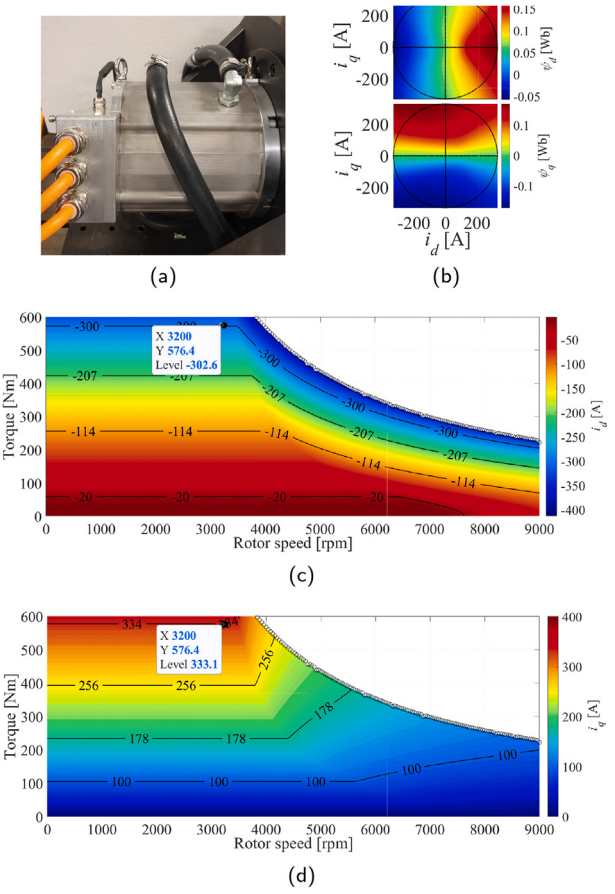

Fig. 9. (a) Picture of the laboratory PMSM used for the electric drive model of this study and its design parameters: (b) flux linkage maps ψ_d and ψ_q, (c) d-axis and (d) q-axis reference current.

Since the purpose of the Matlab/PLECS model is the calculation of the inverter losses, the development of an equivalent thermal network is important in order to have accurate loss estimation for the correct temperature that the inverter experiences. The results from the CHT computations of the previous subsection can be utilized to build an equivalent thermal model of the inverter's cooling system, which is a combined Cauer and Foster network proposed in Ref. [42].

The equivalent thermal model is shown in Fig. 8 and its upper branch is a Foster network. The junction temperature of the MOSFETs T_j is calculated through a junction-to-case thermal resistance-and-capacitance-chain having as input the case temperature T_c. The value of T_c comes from the lower thermal network that has a heat flow source modelling the power losses of the power switches.

The variable $R_{th\ sa}$ represents the thermal resistance between the aluminium cooling plate and the coolant fluid. $R_{th\ cs}$ is the thermal resistance between case and sink, because of the thermal interface material (TIM) and the contact resistance between the bottom side of the power modules and the cooling plate. The TIM affects the heat spreading in the module and $R_{th\ cs}$ is important to be included in the thermal simulation model.

$$R_{th\ cs} = \frac{L}{k A_{contact}} = \frac{R_{th\ cs\ sw}}{n_{sw}} \tag{10}$$

$$R_{th\ sa} = \frac{1}{h_{sa} A_c} \tag{11}$$

where $A_{contact}$ is the total area of the power modules' baseplate, L the thickness of the TIM. Detailed instructions regarding the recommended mounting process of the power modules on the heatsink in order to minimize the $R_{th\ cs}$ can be found in Ref. [43]. However, the resultant thermal resistance value is not available for the specific power modules and instead its value is taken from Refs. [39] for IGBT power modules of similar dimensions and current rating. $R_{th\ cs\ sw} = 0.026$ K/W is the cited case-sink resistance per individual switch position of the inverter. Since the inverter has n_{sw}=6 power switches, a resistance value equal to $4.3 \cdot 10^{-3}$ has been used for the analysis of this paper. A_c is the total surface of the heatsink cooling channel in contact with the coolant.

The thermal capacitance of the cooling plate is calculated as

$$C_{th\ s} = c_p\, m_h. \tag{12}$$

The conduction losses of the SiC MOSFETs and their body diodes are calculated with the PLECS block periodic average, while periodic impulse average is used for the switching losses. It should be noted that synchronous rectification has not been applied in this paper to utilize the reverse conduction capability of the MOSFETs and to further reduce the switching losses of the body diodes. The developed thermal model is a closed loop system, due to the feedback of the inverter's temperature in the power loss calculation and, therefore, the losses are accurately estimated at the correct temperature for each simulated operating point. The transient 3D CHT model in the next Section will provide an even more accurate thermal representation of the heatsink having as input the power losses calculated here.

The Matlab/PLECS model of the drive is utilized for the simulation of an acceleration of the BEV from standstill up to the maximum speed of the drivetrain, which is $v_{max} = 209$ km/h. Since the maximum peak current of the CAB450M12XM3 power module is 450 A, the maximum torque that can be simulated by the electric drive is 580 Nm, which corresponds to approximately this current amplitude as pointed out in Fig. 9(c)–(d). The performance of the inverter is also tested with legislative driving profiles in order to demonstrate the power losses and temperature of the inverter during typical driving conditions. The test cycles chosen for the analysis of this paper are the WLTC [26], which is currently the main drive test procedure for light-duty vehicles in many countries including the EU, and the CLTC [27], which is expected to be applied in the future in China. The WLTC_Class3 cycle and the CLTC_P, which is aimed for light-duty passenger vehicles, are shown in Fig. 10.

The calculated $P_{loss}(t)$ of each power module for each of these cases is later used in Section 4 for the 3D CFD model when running transient CHT computations of the inverter's heatsink. This last design step will help to evaluate the utilization of the heatsink and

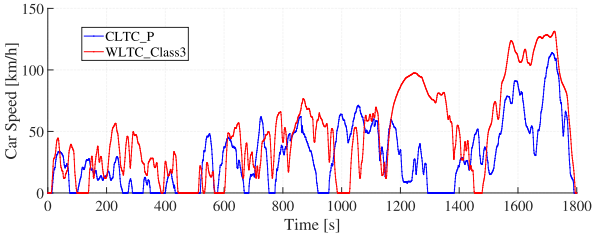

Fig. 10. Speed profile of a vehicle based on the CLTC_P and the WLTC_Class3 driving cycle.

the maximum temperature that it reaches for the specific driving cycles studied here.

4. Results of transient 3D CHT computations

The results of the final heatsink design with rectangular pins (Fig. 5) are shown in this section, while the load of the modelled inverter is dynamically changing. The results obtained from the transient 3D CHT analysis of the inverter are compared with the constant-load 3D CHT computations and the thermoelectrical model in Matlab/PLECS. The performance of the designed heatsink is also evaluated.

Firstly, the acceleration test of the BEV (with parameters displayed in Table 1) is performed, when an initial constant torque of 580 Nm is applied. Then, the results from the tested official driving cycles [26,27] are presented and in this case the required torque for the PMSM is computed with a "backwards" approach [44]. This means that the vehicle acceleration and PMSM torque are calculated having as input the speed profile of the cycles from Fig. 10.

4.1. Acceleration test of the BEV with maximum torque

The acceleration profiles under-test are analysed for inlet coolant temperatures T_{in} equal to 26.85 °C (300 K) and 655 °C, in order to model driving conditions, when the BEV operates at a cool or a warmer environment, respectively. It has been assumed that the T_{in} remains constant throughout the whole test procedure. Conforming with the usual practice in light duty vehicle cooling systems, 6.8 l/min coolant volume flow is used, similar to Refs. [10]. The suitable heat transfer coefficient h_{sa} is obtained from the 3D CHT results of Fig. 6 and is equal to $h_{sa\ 26.85} = 2228.41$ W/(m^{2}K) and $h_{sa\ 65} = 2279.21$ W/(m^{2}K).

The motor accelerates at the beginning and constant torque is applied equal to $T_{m\ max} = 580$ Nm following the reference current given by the MTPA control [Fig. 9(a)–(b)]. When the controller of the inverter reaches its voltage limit and enters the medium- and high-speed regions, the MTPA cannot be followed [40] and the applied torque starts to reduce. Then, the motor operates with constant voltage equal to its maximum value, while the current changes. At $t = 5.2$ s the system reaches its maximum power and the inverter experiences also its maximum losses and temperature.

The results from the acceleration test are shown in Fig. 11, showing that the modelled BEV can accelerate to 100 km/h in 6 s. The semiconductor losses are shown in Fig. 11(c) for both tested coolant temperatures and it can be observed that the increase of the temperature T_{in} leads to higher losses of up to 16.3%. The highest junction temperature T_j is observed at 5.2 s, which is the moment when the motor reaches its peak power. The average temperatures of the power modules' case, sink and junction are shown in Fig. 11(d)–(e). Due to the thermal capacitance of the cooling plate, the highest recorded sink temperature T_s is at approximately 15 s.

The results from the transient 3D CHT model are shown in Fig. 12 for the same acceleration profile. The hottest temperature of the heatsink is reached at 10 s, a bit earlier than in the Matlab/PLECS results. It can be seen that the sink temperature obtained by the transient CHT computations in Fig. 12 is much higher than the T_s value obtained from the equivalent-thermal-model-results in Fig. 11(d)–(e). The reason for that is that the variable T_{sw} shows the average temperature of the area where the power modules are placed, while the temperature T_s represents the whole heatsink which is considered as a single-point in the equivalent thermal model. The junction temperature is also expected to be higher than the obtained values in Fig. 11(d)–(e).

The equivalent thermal model is further fine-tuned by feeding-back into the PLECS model the CHT-calculated case temperatures in order to calculate more accurately the junction temperatures. The resultant new junction temperatures for each individual power module T_j' are shown in Fig. 12 with dotted curves. Especially, for the case with $T_{in} = 65$ °C, the T_j' of the second power module slightly surpasses the 17 °C, which is the maximum allowed temperature of the specific product.

The discrepancy between the individual junction temperatures of the three power modules can also be observed. For example, as can be seen in Fig. 12(a), at 10 s the temperature rise of T_{j2}' (with respect to the T_{in}) is 7.4% and 8.8% higher than the temperature rise of T_{j1}' and T_{j3}', respectively. In a heatsink without uniform heat distribution such as the one shown in Fig. 4, this discrepancy could also be a potential cause of failure for the inverter and faster aging of the hotter semiconductors.

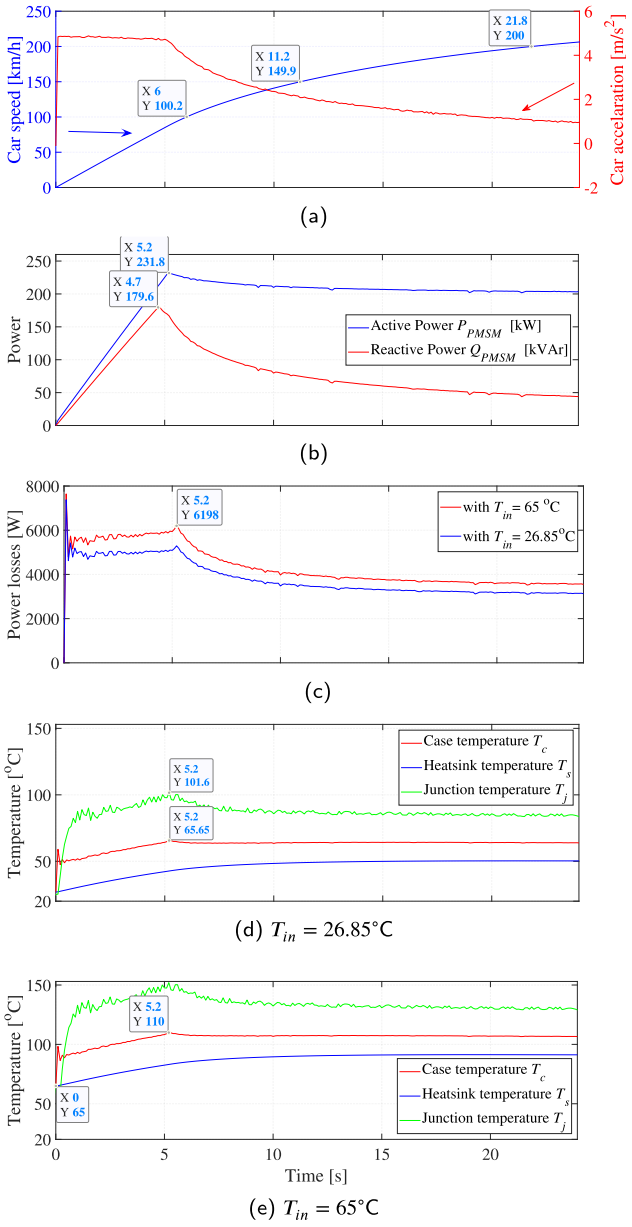

Fig. 11. Results of the (a) speed and acceleration of the BEV when maximum torque is applied, (b) active and reactive power of the motor and (c) semiconductor losses of the inverter, (d)–(e) temperatures of the junction, case and heatsink for different inlet coolant temperatures T_{in}.

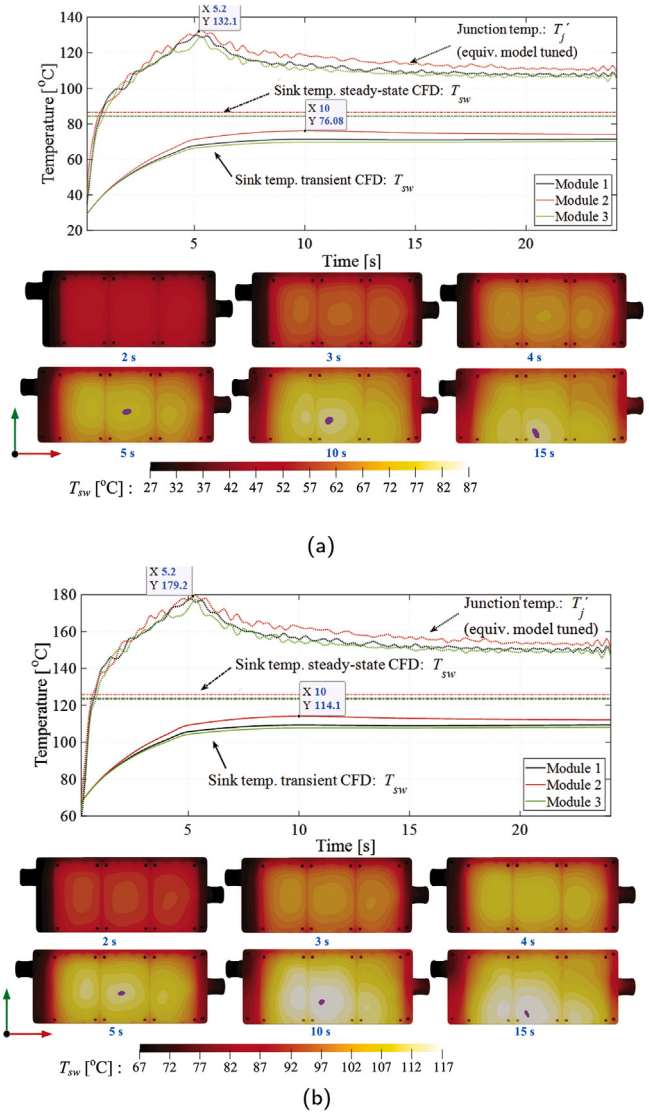

Fig. 12. 3D CHT results during acceleration of the BEV with maximum motor torque in comparison with the corresponding results from the steady-state method, when (a) T_{in} = 26.85 °C and (b) T_{in} = 65 °C.

Fig. 12 also compares the heatsink temperature variation of the proposed design method with that obtained by the conventional steady-state technique (straight dashed-dotted lines), which has been shown previously in Fig. 6(b) for 6.8 l/min coolant flow speed. As can be seen, the sink temperature values which are estimated with the steady-state design method are higher than the ones obtained with the transient CHT computations, throughout the whole acceleration phase of the vehicle. It should be noted that the steady-state calculations refer to 4 kW semiconductor losses, while the computation results by the proposed transient 3D CHT design technique correspond to dynamic power loss of the SiC inverter up to 6.2 kW [Fig. 11(c)]. Designing the heatsink with the conventional steady-state approach to have 6.2 kW of thermal load would lead to an oversized cooling plate, whereas the design with the new transient technique has been accurately tailored to the exact acceleration requirements of the examined electric vehicle. Therefore, it gives the margin for further dynamic overload with additional losses even up to 55% for a duration of almost 10 s until the T_j' safety limit of 175 °C is reached. This means that the new design attains better exploitation of the inverter at the dynamic

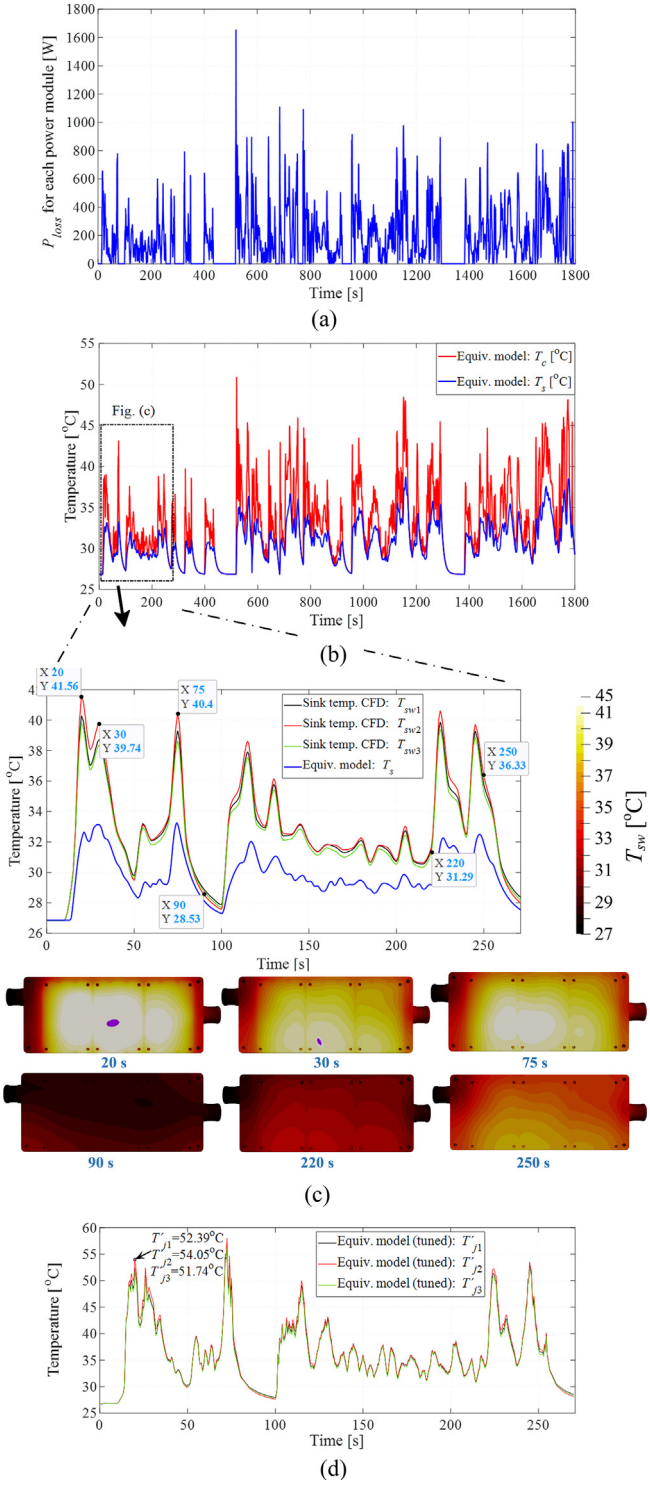

Fig. 13. CLTC_P driving cycle results: (a) power losses for each of the three power modules (b) heatsink temperatures from the thermoelectric system model and (c) individual power module temperatures obtained from the 3D CHT analysis with T_{in} = 26.85 °C and (d) junction temperatures based on the CHT results.

operation, that is a highly critical requirement for an electric vehicle.

4.2. Driving cycle tests with transient CHT computations

The results from the driving cycles tests are shown in Fig. 13 for the CLTC_P and in Fig. 15 for the WLTC_Class3 driving cycle. The

inlet coolant temperature in both cases is equal to $T_{in} = 26.85$ °C and the coolant volume flow is 6.8 l/min. The semiconductor losses and temperatures are shown in these figures.

Specifically for the CLTC_P cycle, Fig. 13(a)–(b) shows the results from the Matlab/PLECS model. A closer look of the first 271 s of the CLTC_P cycle is shown in Fig. 13(c)-(d), where the results of the equivalent thermal model are compared with the transient 3D CHT computations. The average temperature of each power module patch T_{sw} is shown separately and screenshots of the cooling plate can be seen for some characteristic time moments.

Similarly to the acceleration test of the previous subsection, it can be observed that there is a considerable difference between the average sink temperature T_s obtained from the Matlab/PLECS model and the individual temperatures of the power modules T_{sw1}, T_{sw2} and T_{sw3}. The same tuning methodology of the equivalent thermal model is used by feeding into the PLECS model the temperature measurements from the 3D CFD analysis and the resultant junction temperatures of the cycle T'_j are shown in Fig. 13(d). The dynamic response of the two models is also different and for example the temperatures T_{sw} at 20 s are higher compared to the temperatures at 30 s, while the opposite result can be seen in the T_s graph.

The temperature T_{sw2} is the highest most of the time, except for some time instants during the deceleration phase of the cycle such as at 50 s and at 90 s. Then, the T_{sw2} is the lowest temperature among the three. The same results can also be seen for the junction temperatures. The reason for this is that the flow of the coolant and the turbulence in the heatsink change as shown in Fig. 14, where the turbulence kinetic energy k can be seen in the cooling channels of the heatsink as a cursor of the mixing of the fluid. This verifies that the 3D modelling of the heatsink during dynamic load conditions is important in order to capture the exact thermal behavior of the inverter with the smallest possible error. The highest temperature discrepancy between the three power modules is seen at 20 s, when the temperature rise of T'_{j2} (with respect to the T_{in}) is 6.5% and 9.3% higher than the temperature rise of T'_{j1} and T'_{j3}, respectively. The temperature discrepancy between the three modules creates also a difference in their aging process and, in case the reliability data of the chosen semiconductors is available, the exact difference in their spent lifetime can be estimated. For example by considering the Wöhler curve in Ref. [45] for the measured junction temperatures of the simulated CLTC_P cycle, power module 2 has 0.4% and 1.1% higher spent lifetime compared to the modules 1 and 3, respectively. A similar analysis can be implemented for the WLTC cycle shown in Fig. 15.

Another interesting observation is that the hottest area of the cooling plate (pinpointed with a purple dot) is close to the middle of the device, while the temperature keeps increasing until it reaches its peak value, such as at the time moment 20 s when the hotspot-temperature is 43°C. Afterwards, when the temperature starts to decrease, the hottest area moves towards the bottom of the plate, such as at 30 s when the purple dot is 20 mm further down. The same observation can be made for the acceleration speed profile in Fig. 12, where the hottest area of the plate is in the middle up to the 10 s. The consequence of this is that, depending on the operation of the vehicle different areas of the power modules experience the highest temperature affecting also the lifetime of the corresponding semiconductors. Therefore, the transient 3D CHT computations are important in order to study these thermal heterogeneities and to try to tune accordingly the inverter design.

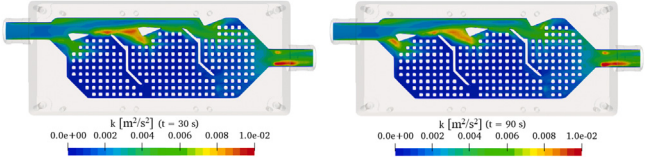

Fig. 14. Turbulence kinetic energy of the heatsink with the CLTC_P cycle at 30 s (left) and 90 s (right).

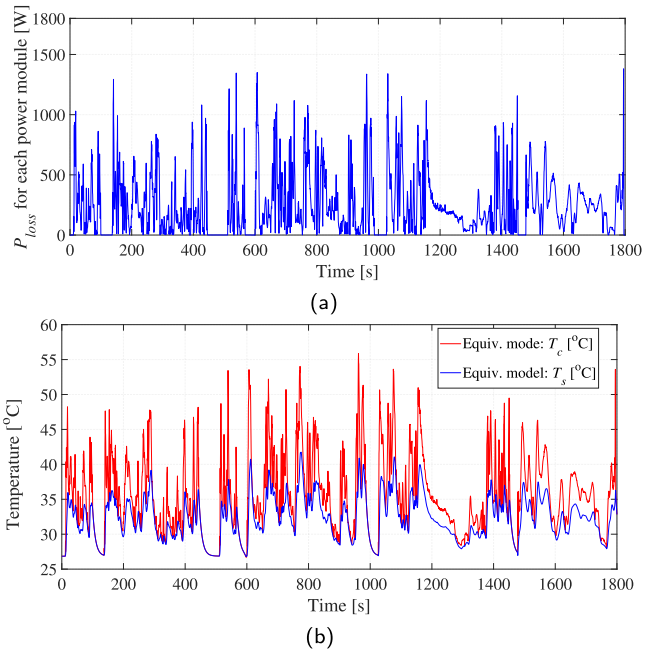

Fig. 15. WLTC_Class3 driving cycle: (a) inverter losses and (b) heatsink temperatures simulated with the thermoelectric system model with $T_{in} = 26.85$ °C.

5. Conclusion

A novel design method for heatsinks of high-power SiC inverter that utilizes transient 3D CHT computations has been presented in this article. The inverter is intended to be used in traction applications and, therefore, an electric vehicle has been modelled in order to verify the proposed design technique. A steady-state 3D CHT model is used for the initial dimensioning of the heatsink with the maximum continuous load. Transient CHT computations are then applied, where the inverter design is evaluated with time-varying load, such as in abrupt acceleration tests of the vehicle and legislative driving cycles. The inverter losses are calculated through a fine-tuned equivalent thermoelectric model of the whole machine drive for all the test cases, while a 3D representation of the sink temperature is computed to show the exact thermal distribution stress of the inverter.

The main advantages of the proposed time-dependent design process are presented in comparison with the commonly used steady-state CHT analysis. Based on the results of the paper, these can be summarized as follows:

1. Firstly, the overload capacity of the designed inverter can be more easily evaluated with the proposed design method, when the maximum acceleration of the investigated vehicle is applied. The results of the paper have shown that short-time overloading with an increase of the thermal heat up to 55% still keeps the heatsink temperature beneath the safety limits, which are defined by the steady-state analysis at maximum load.
2. The transient CHT model can also reveal more accurately the temperature discrepancies among the three SiC power modules during realistic operating conditions, which can reach up to 9.3%

for the tested automotive inverter. This discrepancy is higher than the value obtained when steady-state CHT analysis of the inverter is applied.

3. The transient 3D design method estimates also better the location of the hotspots at the surface of the sink can be calculated, which are actually time-dependent when variable load is applied in the inverter. This can allow more fine-tuned design of the heatsink in order to reduce large temperature differences at the surface of the sink.

It can be finally concluded that time-dependent fluid mechanics and thermal modelling, electromagnetic design and machine control are combined in this paper through the proposed design process in order to provide a tailored-on-demand heatsink. The heatsink design of traction inverters is a multiphysics problem that cannot be accurately represented with equivalent models or just constant-heat computations, since a vehicle operates always with time-varying load. Also, the comparative analysis of the proposed design tool with the commonly-used steady-state design approach has been possible due to the 3D CHT model of the heatsink that allows the calculation of variables such as the inner temperatures of the system and the flow of the coolant, which cannot be easily measured on experimental prototypes without high uncertainly or affecting the system performance with multiple sensors.

CRediT authorship contribution statement

Georgios Mademlis: Conceptualization, Methodology, Writing - original draft. **Raik Orbay:** Methodology, Software, Writing - original draft. **Yujing Liu:** Writing - review & editing, Supervision, Funding acquisition. **Nimananda Sharma:** Methodology, Writing - review & editing. **Rickard Arvidsson:** Writing - review & editing. **Torbjörn Thiringer:** Writing - review & editing.

Declaration of competing interest

The authors declare that they have no known competing financial interests or personal relationships that could have appeared to influence the work reported in this paper.

Acknowledgements

This work has received financial support by the Swedish Energy Agency.

References

[1] Rajashekara K. Present status and future trends in electric vehicle propulsion technologies. IEEE Journal of Emerging and Selected Topics in Power Electronics 2013;1(1):3–10. https://doi.org/10.1109/JESTPE.2013.2259614.

[2] H. S. Seo, D. Shin, Development of parallel and direct cooling system for EV/FCEV inverter (No. 2018-01-0454), SAE Technical Paper, 2018. doi:10.4271/2018-01-0454.

[3] A. Carriero, M. Locatelli, K. Ramakrishnan, G. Mastinu, M. Gobbi, A review of the state of the art of electric traction motors cooling techniques (No. 2018-01-0057), SAE Technical Paper, 2018. doi:10.4271/2018-01-0057.

[4] Jung C. Power up with 800-V systems: the benefits of upgrading voltage power for battery-electric passenger vehicles. IEEE Electrification Magazine 2017;5(1):53–8. https://doi.org/10.1109/MELE.2016.2644560.

[5] Schulz SE. Exploring the high-power inverter: reviewing critical design elements for electric vehicle applications. IEEE Electrification Magazine 2017;5(1):28–35. https://doi.org/10.1109/MELE.2016.2644281.

[6] Merkert A, Krone T, Mertens A. Characterization and scalable modeling of power semiconductors for optimized design of traction inverters with Si- and SiC-devices. IEEE Trans Power Electron 2014;29(5):2238–45. https://doi.org/10.1109/TPEL.2013.2294682.

[7] Olejniczak K, McNutt T, Simco D, Wijenayake A, Flint T, Passmore B, Shaw R, Martin D, Curbow A, Casady J, Hull B. A 200 kVA electric vehicle traction drive inverter having enhanced performance over its entire operating region. In: Proc. 2017 IEEE 5th workshop on wide bandgap power devices and applications. WiPDA); 2017. p. 335–41. https://doi.org/10.1109/WiPDA.2017.8170569.

[8] Zhang C, Srdic S, Lukic S, Kang Y, Choi E, Tafti E. A SiC-based 100 kW high-power-density (34 kW/L) electric vehicle traction inverter. In: Proc. 2018 IEEE energy conversion congress and exposition (ECCE); 2018. p. 3880–5. https://doi.org/10.1109/ECCE.2018.8558373.

[9] K. Namiki, K. Murota, M. Shoji, High performance motor and inverter system for a newly developed electric vehicle (No. 2018-01-0461), SAE Technical Paper, 2018. doi:10.4271/2018-01-0461.

[10] Numakura K, Emori K, Yoshino Y, Hayami Y, Hayashi T. Direct-cooled power module with a thick Cu heat spreader featuring a stress-suppressed structure for EV/HEV inverters. In: Proc. 2016 IEEE energy conversion congress and exposition (ECCE); 2016. p. 1–5. https://doi.org/10.1109/ECCE.2016.7855049.

[11] Zhou Z, Kanniche MS, Butcup SG, Igic P. High-speed electro-thermal simulation model of inverter power modules for hybrid vehicles. IET Electr Power Appl 2011;5(8):636–43. https://doi.org/10.1049/iet-epa.2011.0048.

[12] Kersten A, Grunditz E, Thiringer T. Efficiency of active three-level and five-level NPC inverters compared to a two-level inverter in a vehicle. In: Proc. 2018 20th European conference on power electronics and applications (EPE'18 ECCE europe); 2018. P.1–9. https://ieeexplore.ieee.org/document/8515355.

[13] Tang C, Thiringer T. Thermal modelling of a mutlichip IGBT power module. In: Proc. 2019 21st European conference on power electronics and applications (EPE '19 ECCE europe); 2019. P.1–8. https://doi.org/10.23919/EPE.2019.8914769.

[14] Song Y, Wang B. Evaluation methodology and control strategies for improving reliability of HEV power electronic system. IEEE Trans Veh Technol 2014;63(8):3661–76. https://doi.org/10.1109/TVT.2014.2306093.

[15] Arfa Grunditz E, Thiringer T. Electric vehicle IGBT power module sizing and drive cycle energy efficiency for various switching frequencies-based on a scalable module model. In: Proc. 2018 20th European conference on power electronics and applications (EPE'18 ECCE europe). IEEE; 2018. P.1–10. https://ieeexplore.ieee.org/document/8515390.

[16] Shahjalal M, Ahmed R, Lu H, Bailey C, Forsyth A. An analysis of the thermal interaction between components in power converter applications. IEEE Trans Power Electron 2020;35(9):9082–94. https://doi.org/10.1109/TPEL.2020.2969350.

[17] Baumann H, Heinemeyer P, Staiger W, Topfer M, Unger K, Muller D. Optimized cooling systems for high-power semiconductor devices. IEEE Trans Ind Electron 2001;48(2):298–306. https://doi.org/10.1109/41.915408.

[18] Nakatsu K, Saito R. The next-generation high power density inverter technology for vehicle. In: Proc. 2014 international power electronics conference (IPEC-Hiroshima 2014 - ECCE ASIA); 2014. p. 1925–8. https://doi.org/10.1109/IPEC.2014.6869850.

[19] Olesen K, Bredtmann R, Eisele R. "ShowerPower" new cooling concept for automotive applications. In: Proc. of the automotive power electronics conference. -; June, 2006. p. 21–2. Paris, France, https://www.researchgate.net/profile/Klaus_Olesen/publication/267305118_ShowerPower_New_Cooling_Concept_for_Automotive_Applications/links/57552d6608ae02ac12811c62/ShowerPower-New-Cooling-Concept-for-Automotive-Applications.pdf.

[20] Reeves M, Moreno J, Beucher P, Loong S-J, Brown D. Investigation on the impact on thermal performances of new pin and fin geometries applied to liquid cooling of power electronics. In: Proc. PCIM europe; 2011. p. 772–8.

[21] Zhang J, Zhu X, Mondejar ME, Haglind F. A review of heat transfer enhancement techniques in plate heat exchangers. Renew Sustain Energy Rev 2019;101:305–28.

[22] N. Karras, T. Kuthada, J. Wiedemann, An approach for water jacket flow simulations (No. 2014-01-0659), SAE Technical Paper, 2014. doi:10.4271/2014-01-0659.

[23] Wang L, Qin Z, Dong J, Bauer P. Design, modelling and evaluation of a GaN based motor drive for a solar car. In: Proc. IECON 2019 - 45th annual conference of the IEEE industrial electronics society, vol. 1; 2019. p. 5120–5. https://doi.org/10.1109/IECON.2019.8927042.

[24] K. Haehndel, A. Pere, T. Frank, F. Christel, S. Abanteriba, A numerical investigation of dampening dynamic profiles for the application in transient vehicle thermal management simulations (No. 2014-01-0642), SAE Technical Paper, 2014. doi:10.4271/2014-01-0642.

[25] H. Reister, W. Bauer, Simulation process of the heat protection of a full vehicle (No. 2012-01-0635), SAE Technical Paper, 2012. doi:10.4271/2012-01-0635.

[26] Tutuianu M, Bonnel P, Ciuffo B, Haniu T, Ichikawa N, Marotta A, et al. Development of the World-wide harmonized Light duty Test Cycle (WLTC) and a possible pathway for its introduction in the European legislation. Transport Res Transport Environ 2015;40:61–75. https://doi.org/10.1016/j.trd.2015.07.011.

[27] Standardization Administration of China. China automotive test cycle—Part 1: light-duty vehicles GB/T 38146.1-2019. -; 2020.

[28] Wolfspeed Power & Rf. CAB450M12XM3. 2019 [Online], accessed 2020-07-03. Available at: https://www.wolfspeed.com/media/downloads/1493/CAB450M12XM3.pdf.

[29] Grunditz E. Design and assessment of battery electric vehicle powertrain, with respect to performance, energy consumption and electric motor thermal capability. Doctoral thesis. Gothenburg, Sweden: Chalmers University of Technology; 2016. https://research.chalmers.se/en/publication/236616.

[30] Incropera FP, Lavine AS, Bergman TL, DeWitt DP. Fundamentals of heat and mass transfer. Wiley; 2007.

[31] Bejan A, Kraus AD. Heat transfer handbook, vol. 1. John Wiley & Sons; 2003.
[32] OpenFOAM [Online], accessed 2020-07-03. Available at: https://openfoam.org/; 2020.
[33] Li Y. Implementation of multiple time steps for the multi-physics solver based on chtmultiregionfoam, CFD with. OpenSource software 2016. http://www.tfd.chalmers.se/~hani/kurser/OS_CFD_2016/YuzhuPearlLi/final_report_Jan2017.pdf.
[34] CFD Direct. Energy equation in OpenFOAM. 2016. accessed 2020-07-03. Available at: https://cfd.direct/openfoam/energy-equation/.
[35] OpenFOAMwiki. Chtmultiregionfoam. 2019. accessed 2020-07-03. Available at: https://openfoamwiki.net/index.php/ChtMultiRegionFoam.
[36] Menter FR. Two-equation eddy-viscosity turbulence models for engineering applications. AIAA Journal 1994;32(8):1598–605. https://doi.org/10.2514/3.12149.
[37] Qian C, Gheitaghy AM, Fan J, Tang H, Sun B, Ye H, et al. Thermal management on IGBT power electronic devices and modules. IEEE Access 2018;6:12868–84. https://doi.org/10.1109/ACCESS.2018.2793300.
[38] Hitachi T, Gohara H, Nagaune F. Direct liquid cooling IGBT module for automotive applications. Fuji Electr Rev 2012;58(2):55–9. https://www.fujielectric.com/company/tech/pdf/58-02/FER-58-2-055-2012.pdf.
[39] A. Wintrich, Thermal resistance of IGBT modules-specification and modelling, Semikon Application Note, AN1404, 2014.
[40] Tang J. Synchronous machines with high-frequency brushless excitation for vehicle applications. Gothenburg, Sweden: Licentiate thesis, Chalmers University of Technology; 2019. https://research.chalmers.se/en/publication/512640.
[41] Harnefors L. Control of variable-speed drives, applied signal processing and control. Department of Electronics, Mälardalen University; 2002. https://books.google.se/books/about/Control_of_Variable_speed_Drives.html?id=wyXXjwEACAAJ&redir_esc=y.
[42] Ma K, Liserre M, Blaabjerg F, Kerekes T. Thermal loading and lifetime estimation for power device considering mission profiles in wind power converter. IEEE Trans Power Electron 2015;30(2):590–602. https://doi.org/10.1109/TPEL.2014.2312335.
[43] Wolfspeed XM3. Thermal interface material application note. CPWR-AN29; 2019. Rev. A [Online], accessed 2020-10-12. Available at: https://www.wolfspeed.com/downloads/dl/file/id/1504/product/482/xm3_thermal_interface_material_guide.pdf.
[44] Gao DW, Mi C, Emadi A. Modeling and simulation of electric and hybrid vehicles. Proc IEEE 2007;95(4):729–45. https://doi.org/10.1109/JPROC.2006.890127.
[45] Infineon Technologies, PC and TC Diagrams, Infineon application note, AN2019-05 Revision 2.0, 2020.